

Predicting surface oscillations in Lake Superior from normal mode dynamics



Samuel M. Kelly^a Maqsood Mansur^a, and Erica Green^a

^aLarge Lakes Observatory and Physics & Astronomy Department, University of Minnesota
Duluth, Duluth, Minnesota

Corresponding author: Samuel M. Kelly, smkelly@d.umn.edu

Early Online Release: This preliminary version has been accepted for publication in *Journal of Physical Oceanography*, may be fully cited, and has been assigned DOI 10.1175/JPO-D-23-0079.1. The final typeset copyedited article will replace the EOR at the above DOI when it is published.

© 2023 American Meteorological Society. This is an Author Accepted Manuscript distributed under the terms of the default AMS reuse license. For information regarding reuse and general copyright information, consult the AMS Copyright Policy (www.ametsoc.org/PUBSReuseLicenses).

ABSTRACT: Satellite observation of sea surface height (SSH) may soon have sufficient accuracy and resolution to map geostrophic currents in Lake Superior. A dynamic atmosphere correction will be needed to remove SSH variance due to basin-wide seiching. Here, the dynamics of rotating barotropic gravity modes are examined using numerical models and lake-level gauges. Gravity modes explain 94% of SSH variance in a general circulation model, and evolve as forced, damped oscillators. These modes have significant SSH, but negligible kinetic energy (2 J m^{-2}) and dissipation rates (0.01 W m^{-2}) relative to other motions in Lake Superior. Removing gravity modes from instantaneous SSH allows geostrophic currents to be accurately computed. Complex empirical orthogonal functions (CEOFs) from 50 years of data at 8 lake-level gauges show patterns consistent with the first two gravity modes. The frequency spectra of these CEOFs are consistent with forced, damped oscillators with natural frequencies of 3.05 and 4.91 cycles per day and decay time scales of 4.5 and 1.0 days. Modal amplitudes from the general circulation model and lake-level gauges are 80% coherent at 1 cpd, but only 50% coherent at 3 cpd, indicating that the atmospheric reanalysis used to force the general circulation model is not accurate at the high natural frequencies of the gravity modes. The results indicate that a dynamic atmosphere correction should combine modeled gravity modes below 1 cpd and observed mode-1 and 2 amplitudes (from lake-level gauges) at higher frequencies. An inverted barometer correction is also recommended to account for low-frequency atmospheric pressure gradients that do not project onto gravity modes.

1. Introduction

Predictions of sea surface height (SSH)¹ in semi-enclosed seas and large lakes have great societal value. Long term changes in sea levels (Nicholls and Cazenave 2010) and lake levels (Prange et al. 2020) have major impacts on coastal communities. For example, the decreasing level of Lake Malawi threatens Malawi's energy production, irrigation, drinking water, and fisheries (Kumambala and Ervine 2010). Here we focus on shorter timescale SSH dynamics, which are driven by wind and atmospheric pressure. These dynamics include quasi-geostrophic circulation, wind setup, inverted barometer, tides, seiches, meteotsunamis, and wind waves (e.g., Csanady 1982; Woodworth et al. 2019). These motions directly affect coastal infrastructure (Meadows et al. 1997), wetland ecology (Trebitz 2006), and public safety (Monserrat et al. 2006). For example, meteotsunamis with heights greater than 0.3 m occur more than 100 times per year in the Laurentian Great Lakes (Bechle et al. 2016), occasionally killing people (Ewing et al. 1954). Meteotsunamis are also common in the coastal ocean (Angove et al. 2021).

SSH also determines geostrophic surface currents, which are prevalent in large lakes (e.g., Saylor and Miller 1987; Boyce et al. 1989; Beletsky et al. 1999; Bennington et al. 2010; Beletsky et al. 2013) and semi-enclosed seas (Lebedev 2018; Taqi et al. 2019). Surface currents transport pollutants, harmful algae, microplastics, people lost at sea, larvae and heat. These transports impact recreation (Nevers et al. 2014), fisheries (through per- and polyfluoroalkyl substances and microplastics contamination; Remucal 2002; Cox et al. 2021), and drinking water (Sayers et al. 2019). Surface geostrophic currents are routinely computed in the open ocean from satellite observations of SSH (Le Traon and Morrow 2001), but the accuracy and resolution of these observations are only sufficient to map currents in the Red Sea (Taqi et al. 2019) and Caspian Sea (Lebedev 2018), which are about five times larger than Lake Superior. Thus, satellite altimetry over Lake Superior has historically only been used to monitor water levels (Morris and Gill 1994). The Surface Water Ocean Topography (SWOT) mission will improve SSH resolution by a factor of 5-10 (i.e., the largest resolved scale should be reduced from 150 km to 15-30 km; Morrow et al. 2019), finally making it possible to map geostrophic currents in the Great Lakes and other small enclosed and semi-enclosed seas.

¹Throughout, we use SSH for both seas and lakes.

a. Estimating surface currents from SSH

When the advective and temporal Rossby numbers are small, the momentum balance is approximately linear and steady (Cushman-Roisin and Beckers 2011). The momentum equation averaged over the surface mixed layer is

$$\underbrace{f\hat{\mathbf{k}} \times \bar{\mathbf{u}}_{\text{mix}}}_{I} = \underbrace{-\nabla(g\bar{\eta} + \bar{p}_{\text{atm}})}_{II} + \overline{\tau_s/H_{\text{mix}}}, \quad (1)$$

where an overbar indicates a low-pass filter (or time average), \mathbf{u}_{mix} is the horizontal surface velocity, η is SSH, p_{atm} is atmospheric pressure at the surface (divided by reference density, $\rho_0 = 1000 \text{ kg m}^{-3}$), and τ_s is the wind stress (also divided by reference density). f is the inertial frequency, g is gravity, and H_{mix} is the mixed layer depth. Here, the mixed layer is approximated as a slab model with vertically uniform velocity and stress divergence (Pollard and Millard 1970).

The velocity in (1) can be decomposed into two components: a geostrophic balance between (I) and (II) and an Ekman balance between (I) and (III). Ekman and Geostrophic velocities can also offset each other when (II) and (III) balance such that a lake has setup an SSH gradient that balances the mean wind stress (Simons and Schertzer 1989). “Setup” occurs quickly in enclosed seas, halting barotropic transport, so that during the stratified season most surface currents are baroclinic (Beletsky et al. 1999). In addition, $g\bar{\eta}$ and \bar{p}_{atm} often largely offset each other due to the inverted barometer effect (Wunsch and Stammer 1997). Thus, \bar{p}_{atm}/g is often treated as an atmospheric correction to total SSH, such that the “corrected” SSH purely drives geostrophic motion, $\eta_G = \bar{\eta} + \bar{p}_{\text{atm}}/g$ (e.g., Carrere and Lyard 2003).

b. The dynamic atmosphere correction

The SWOT satellite has a 21 day repeat orbit, so η_G cannot be determined from a simple time average. Instead, η_G must be estimated from each observation of η using a “dynamic atmosphere correction” that removes both the low-frequency inverted barometer effect and high-frequency barotropic oscillations (Carrere and Lyard 2003). Le Traon and Morrow (2001) note that “standard altimetric corrections for the tides and atmospheric pressure response have larger errors in coastal or semi-enclosed seas than in the open ocean” because of complicated bathymetry and the potential for resonant basin-modes. In Lake Superior, tidal SSH can be removed following Sanchez et al.

(1985), but high frequency SSH due to atmospheric forcing needs to be modeled or extrapolated from hourly observations at a network of lake-level gauges. This manuscript will examine the dynamics of high-frequency SSH in Lake Superior using numerical models and lake-level gauges. The long-term aim of this work is to develop a dynamic atmosphere correction specifically for SWOT data over the Great Lakes and other enclosed and semi-enclosed basins. A precise evaluation of this correction requires SWOT data, which will be analyzed in future work.

c. Basin modes

SSH variability in enclosed basins can be decomposed into normal modes for dynamic analysis (e.g., Hutter et al. 2011). In non-rotating basins there is a complete set of orthogonal gravity modes (e.g., Schwab 1980; Rueda and Schladow 2002; As-Salek and Schwab 2004), often called seiches, and a separate set of solenoidal modes (e.g., Rao and Schwab 1981; Rao et al. 1987) that describe steady topographic gyres (Csanady 1982). The Earth's rotation couples these sets, greatly complicating modal analysis, even in simply shaped basins (Rao 1966). The resultant modes form a single spectrum that contains both sub-inertial rotational motions and super-inertial gravity wave motions. Rao and Schwab (1976) developed a method to compute these modes in arbitrarily basins using finite-differences, which crudely represents coastlines as piece-wise constant curves. Steinmoeller et al. (2019) improved this method by using finite elements on a triangular mesh, which allow for high fidelity coastlines. In Lake Superior, the lowest gravity mode is an east-west seiche with a period of about 8 h (Platzman 1972). Higher modes have shorter periods and increasingly complicated spatial structures (Rao and Schwab 1976; Mortimer and Fee 1976; Sanchez et al. 1985). Rotational modes in Lake Superior have periods of several days or longer. They are difficult to interpret because their horizontal structures are complicated and not ordered by period (Rao and Schwab 1976). We take the view that gravity modes provide a convenient basis for studying inertial-gravity wave motions, but rotational modes do not provide any obvious benefit for studying low-frequency circulation. In contrast, the solenoidal modes used by Rao and Schwab (1981) are more useful for describing geostrophic circulation. Internal (reduced-gravity) modes also occur in the Great Lakes and produce upwelling, mixing, and sediment resuspension (e.g., Schwab 1977; Antenucci and Imberger 2001; Mortimer 2006; Valiour et al. 2015; Ahmed

et al. 2014). However, these modes have negligible SSH signals and periods of weeks to months, so they do not play a role in the dynamic atmosphere correction.

Normal modes are useful because, using Galerkin's method, they drastically simplify the equations of motion (e.g. Boyd 2001). Here, we project the equations of motion onto normal modes to obtain a dynamical model that is a forced, damped, harmonic oscillator. This prediction method is not novel and has been applied several times. Hamblin and Hollan (1978) projected the equations of motion onto basin modes for Lake Constance and predicted its SSH from observed atmospheric forcing. Sanchez et al. (1985) predicted SSH in Lake Superior from tidal forcing. Schwab (1982) solved the equations in reverse for Lake Ontario, predicting wind stress from observations of SSH. Shimizu et al. (2007) and Shimizu and Imberger (2008) predicted internal seiches in lakes Biwa and Kinneret, respectively. We also note that dynamical models based on orthogonal modes are less useful when predictions require a superposition of many modes. For example, finite-volume models are better suited to study Helmholtz oscillations between lakes Michigan and Huron (Anderson and Schwab 2013, 2017) and high frequency meteotsunamis in Lake Michigan (Anderson et al. 2015; Anderson and Mann 2021).

d. Outline

The aim of this study is to predict and characterize the dynamics of gravity modes in Lake Superior. The first and second basin-wide gravity modes were previously described by Platzman (1972), Rao and Schwab (1976), and Mortimer and Fee (1976), but, to our knowledge, nobody has synthesized the modal dynamics to actually predict Lake Superior's water level. In the remainder of the article, we review the theory of normal modes (Section 2a), introduce two numerical models of Lake Superior (Section 2b), and describe 50 years of lake level data (Section 2c). Modeling and observational results are described in Sections 3 and 4, respectively. Section 5 presents our conclusions and discusses their implications for a dynamical atmosphere correction to SWOT data.

2. Methods

a. Modal dynamics

Water level dynamics in Lake Superior are well described by the linearized, f -plane, shallow water equations. The condition for linearization is $\eta/H_0 \sim u/\sqrt{gH_0} \ll 1$, which is about 10^{-3} in

Lake Superior because surface displacements are $\eta \sim 10$ cm (Fig. 2) and the mean depth is $H_0 \approx 150$ m (Fig. 1). A shallow water wave speed of $\sqrt{gH_0} \approx 40$ m s⁻¹ implies that currents are $u \sim 3$ cm s⁻¹ when $\eta \sim 10$ cm. The Earth's rotation is important for linear flows when the temporal Rossby number is T_f/T small. The inertial period in Lake Superior is $T_f \approx 16$ h (at 48° N), so oscillations with periods, T , longer than about 4 h will be influenced by rotation. Merian's formula with a basin length of 500 km suggests that the lowest mode in Lake Superior has a period of about 8 h, as observed by Mortimer and Fee (1976). Oscillations in smaller basins have shorter periods and are less influenced by rotation.

The linear, hydrostatic, f -plane, shallow water equations with atmospheric forcing are

$$\partial_t \mathbf{U} + f \hat{\mathbf{k}} \times \mathbf{U} = -g H \nabla \eta - H \nabla p_{\text{atm}} + \boldsymbol{\tau}_s - \boldsymbol{\tau}_b \quad (2a)$$

$$\partial_t \eta = -\nabla \cdot \mathbf{U} \quad (2b)$$

where $\mathbf{U}(\mathbf{x}, t) = (Hu, Hv)$ is the volume transport vector, $\boldsymbol{\tau}_b$ is bottom stress, $H(\mathbf{x})$ is the depth, and \mathbf{x} is horizontal position. The system is completed by lateral boundary conditions that enforce no normal flow, $\mathbf{U} \cdot \hat{\mathbf{n}} = 0$, at solid boundaries and no normal flux, $\eta = 0$, at open boundaries.

Platzman (1972) derived basin modes by analyzing the unforced, undamped system in “primitive” operator form

$$\mathbf{M} \partial_t \mathbf{a} = -i \mathbf{K} \mathbf{a} \quad (3)$$

where

$$\mathbf{a} = \begin{bmatrix} \mathbf{U} \\ \eta \end{bmatrix}, \quad \mathbf{M} = \begin{bmatrix} 1/H & 0 \\ 0 & g \end{bmatrix}, \quad \text{and} \quad \mathbf{K} = i \begin{bmatrix} -\frac{f}{H} \hat{\mathbf{k}} \times & -g \nabla \\ -g \nabla \cdot & 0 \end{bmatrix}. \quad (4)$$

Trying a solution of the form $\mathbf{a}_n e^{-i\omega t}$ (where i is the imaginary number and ω is a frequency) turns the system into a generalized eigenvalue problem

$$\omega_n \mathbf{M} \mathbf{a}_n = \mathbf{K} \mathbf{a}_n . \quad (5)$$

The inner product is

$$\langle \mathbf{a}_m, \mathbf{a}_n \rangle = \frac{1}{A} \int \mathbf{a}_m^{*T} \mathbf{a}_n dA \quad (6)$$

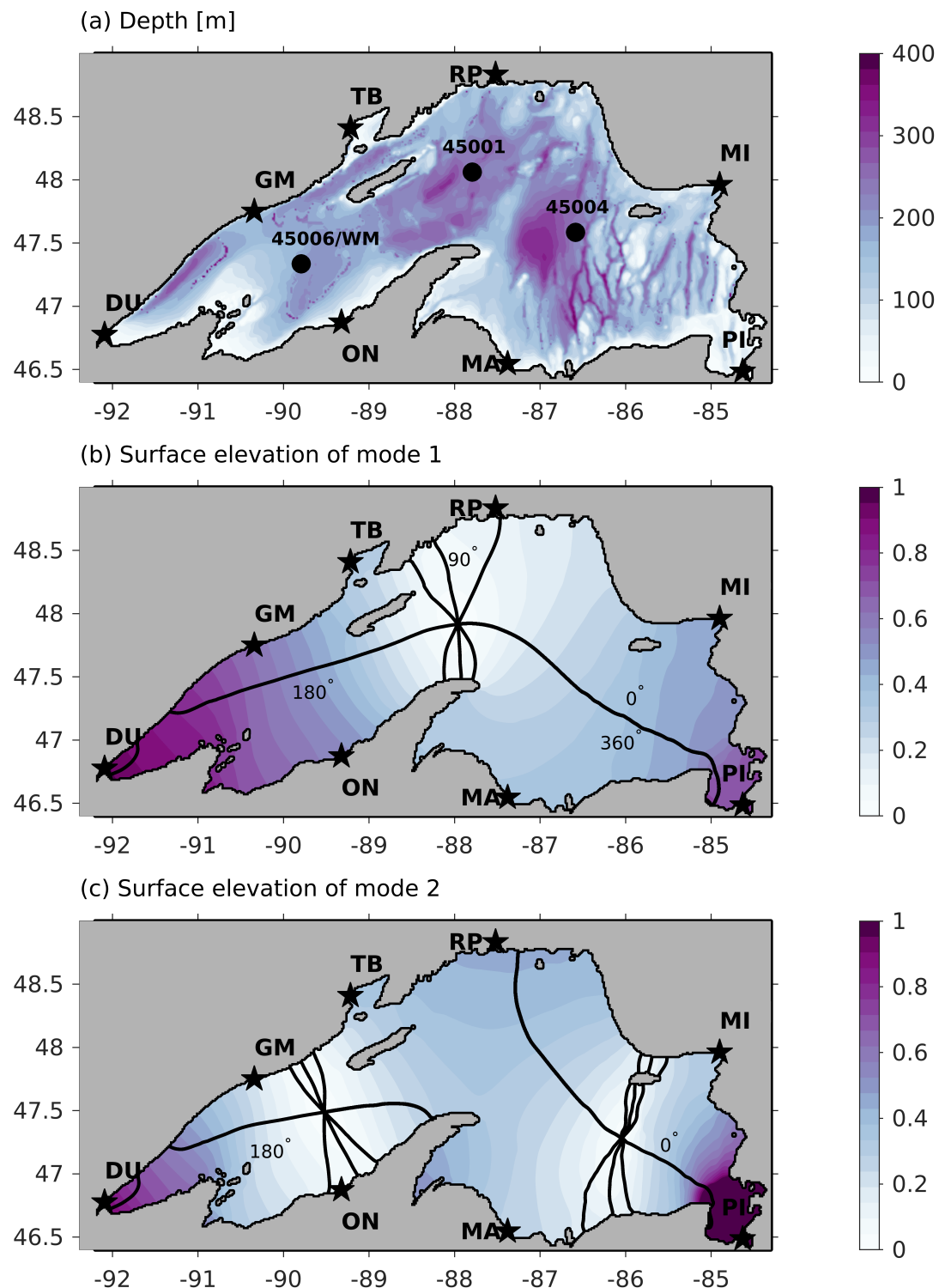


FIG. 1. Depth (a), the first basin mode (3.05 cpd) amplitude and phase (b), and the second basin mode (4.91 cpd) amplitude and phase (c). Stars are lake-level gauges, circles are meteorological buoys.

where A indicates the basin area, $*$ a complex conjugate, and T a transpose. \mathbf{K} is self-adjoint (Hermitian) because

$$\langle \mathbf{a}_m, \mathbf{Ka}_n \rangle - \langle \mathbf{Ka}_m, \mathbf{a}_n \rangle = -\frac{i}{A} \int \nabla \cdot (g\eta_m^* \mathbf{U}_n + g\eta_n \mathbf{U}_m^*) \mathbf{d}A \quad (7a)$$

$$= -\frac{i}{A} \oint \hat{\mathbf{n}} \cdot (g\eta_m^* \mathbf{U}_n + g\eta_n \mathbf{U}_m^*) \mathbf{d}S = 0 \quad (7b)$$

provided the the solutions satisfy the boundary conditions. The second line in (7) follows from the divergence theorem, and establishes that the boundary integral of outward-normal energy flux must be zero. This condition is trivial for an autonomous basin but requires a strong assumption along the open boundaries of a semi-enclosed basin. The modes \mathbf{a}_n must be orthogonal if \mathbf{K} is self-adjoint because

$$\langle \mathbf{a}_m, \mathbf{Ka}_n \rangle - \langle \mathbf{Ka}_m, \mathbf{a}_n \rangle = \langle \mathbf{a}_m, \omega_n \mathbf{Ma}_n \rangle - \langle \omega_m \mathbf{Ma}_m, \mathbf{a}_n \rangle \quad (8a)$$

$$0 = (\omega_n - \omega_m) \frac{1}{A} \int \left(\frac{\mathbf{U}_m^* \cdot \mathbf{U}_n}{H} + g\eta_m^* \eta_n \right) \mathbf{d}A \quad (8b)$$

where the first line follows from (5) and the integral on the second line must be zero whenever $\omega_m \neq \omega_n$. When $m = n$, the modes can be scaled (normalized) so that

$$\langle \mathbf{a}_m, \mathbf{Ma}_n \rangle = \delta_{mn} \left[\frac{\text{m}^3}{\text{s}^2} \right] \quad (9)$$

where δ_{mn} is the Kronecker delta. This orthogonality condition (9) involves a weighted area integral over transport and surface displacement. \mathbf{M} may be interpreted as a metric tensor that scales the inner product so that it (i) combines quantities with consistent dimensions and (ii) returns twice the basin-integrated energy. In an effort to reduce the number of state variables, one can also reformulate the eigenvalue problem (5) in terms of just η , but this is inadvisable when the problem includes rotation (see Rao and Schwab 1976, and Appendix).

Normal modes are useful because they provide an efficient basis for predicting the evolution of a complex system. This derivation roughly follows Hamblin and Hollan (1978). The forced, damped system (2) can be written

$$\mathbf{M}\partial_t \mathbf{a} = -i\mathbf{Ka} + \mathbf{q} - \mathbf{d} \quad (10)$$

where

$$\mathbf{q} = \begin{bmatrix} \frac{\tau_s}{H} - \nabla p_{\text{atm}} \\ 0 \end{bmatrix} \quad \text{and} \quad \mathbf{d} = \begin{bmatrix} \frac{\tau_b}{H} \\ 0 \end{bmatrix} \quad (11)$$

are the forcing and damping vectors, respectively. The state vector is expanded $\mathbf{a}(\mathbf{x}, t) = \sum_{n=1}^{\infty} A_n(t) \mathbf{a}_n(\mathbf{x}) + A_n^*(t) \mathbf{a}_n^*(\mathbf{x})$, where $A_n(t)$ is a dimensionless complex amplitude and the complex conjugate ensures the vector is entirely real [note that solutions to (5) come in conjugate pairs, \mathbf{a}_n and \mathbf{a}_n^* , which are orthogonal $\langle \mathbf{a}_n, \mathbf{M} \mathbf{a}_n^* \rangle = 0$ and have eigenfrequencies ω_n and $-\omega_n$, respectively]. Projecting (10) onto \mathbf{a}_n using the orthogonality condition (9) yields the modal evolution equation

$$\begin{aligned} \langle \mathbf{a}_n, \mathbf{M} \partial_t \mathbf{a} \rangle + \langle \mathbf{a}_n, i \mathbf{K} \mathbf{a} \rangle &= \langle \mathbf{a}_n, \mathbf{q} \rangle - \langle \mathbf{a}_n, \mathbf{d} \rangle \\ \partial_t A_n + i \omega_n A_n &= F_n - D_n . \end{aligned} \quad (12)$$

Note that in the notation used here, $A_n(t) \mathbf{U}_n(\mathbf{x})$ is the transport due to the n^{th} mode [$\mathbf{U}_n(\mathbf{x})$ is the mode shape]. Also note that A_n is dimensionless, but (12) has units $\text{m}^3 \text{ s}^{-2}$ via (9).

The modal forcing is

$$F_n(t) = \langle \mathbf{a}_n, \mathbf{q} \rangle = \frac{1}{A} \int \left[\frac{\mathbf{U}_n^* \cdot \tau_s}{H} - i \omega_n \eta_n^* p_{\text{atm}} \right] dA , \quad (13)$$

after rewriting the pressure term using the divergence theorem, applying the boundary conditions on \mathbf{U}_n , and substituting $\nabla \cdot \mathbf{U}_n^* = -i \omega_n \eta_n^*$. To linearize the problem, we must ignore the surface water velocity when calculating wind stress, even though this can alter wind work (Duhaut and Straub 2006).

The modal damping is

$$D_n(t) = \langle \mathbf{a}_n, \mathbf{d} \rangle = \frac{1}{A} \int \frac{\mathbf{U}_n^* \cdot \tau_b}{H} dA . \quad (14)$$

Bottom stress is typically parameterized as quadratic drag, $\tau_b = C_d |\mathbf{u}| \mathbf{u}$, but this complicates the analysis by coupling the modes (MacKinnon and Winters 2005) and creating a non-linear evolution equation. Spatially variable drag also greatly complicates the analyses (Shimizu and Imberger 2008). Here, we show that a spatially constant linear drag is sufficient to provide accurate predictions (Section 3b). Our ad hoc drag parameterization is, $D_n = r_n A_n$, where r_n is a constant.

This parameterization can be refined at a later date, like the drag parameterization in the TPXO tide model (Egbert et al. 1994; Egbert 1997).

With linear drag, the evolution equation A_n is the canonical damped, forced oscillator in disguise. Multiplying (12) by $(\partial_t + r_n - i\omega_n)$ produces

$$\partial_{tt} A_n + 2r_n \partial_t A_n + (\omega_n^2 + r_n^2) A_n = (\partial_t + r - i\omega_n) F_n \quad (15)$$

which has natural frequency $\sqrt{\omega_n^2 + r_n^2}$, damped frequency ω_n , and quality factor $Q = \omega_n/(2r_n)$. Recall that the amplitude of an unforced oscillation decays by a factor of e after Q/π periods and the bandwidth of the resonant peak is $\Delta\omega = \omega_n/(2Q) = r_n$. The energy balance is obtained by multiplying (12) by $\rho_0 A A_n^*$ and adding the complex conjugate

$$\partial_t (\rho_0 A |A_n|^2) = \rho_0 A (F_n A_n^* + F_n^* A_n) - 2\rho_0 r A |A_n|^2 \quad [\text{W}] , \quad (16)$$

where A is the basin area and A_n is the modal amplitude. The first term in (16) is the energy tendency, the second external work, and the third dissipation.

b. Numerical models

The preceding section reduced SSH dynamics to a set of forced, damped, harmonic oscillators (12), which can be solved by Laplace transform (Morse 1948) or a time-stepping method (we use the 2nd order Adams-Bashforth method; Cushman-Roisin and Beckers 2011). To solve the model for a realistic basin, we must discretize \mathbf{M} and \mathbf{K} on a numerical grid and solve the numerical eigenvalue problem (5). Steinmoeller et al. (2019) developed a highly accurate finite-element method to do this, however, we use Rao and Schwab (1976)'s simpler finite-difference method because it easily resolves the large-scale modes using Smith and Sandwell (1997) bathymetry and our 250-m resolution grid. The first mode has a frequency of 3.05 cycles per day (cpd) and is essentially an east-west seiche with a slight counterclockwise propagation due to rotation (Fig. 1). This mode is indistinguishable from those published by Platzman (1972) (3.06 cpd) and Rao and Schwab (1976) (3.05 cpd). The second (4.9 cpd) and third (6.2 cpd) modes are also similar to those computed by Rao and Schwab (1976) (5.4 and 6.4 cpd), but higher modes are sensitive to

the inclusion/exclusion of long shallow bays and estuaries that support harbor modes (Miles 1974) with periods of a couple hours (Jordan et al. 1981).

To identify shortcomings of the theoretical model, we compare it to the MIT general circulation model (MITgcm; Marshall et al. 1997). An MITgcm simulation was run on a 1-km grid with 22 vertical levels and configured to include advection, a non-linear free surface, quadratic bottom drag ($C_d = 0.001$), variable f (i.e., a β -plane), and realistic summer stratification (Austin and Allen 2011). Horizontal and vertical viscosities of $1 \text{ m}^2/\text{s}$ and $10^{-2} \text{ m}^2/\text{s}$, respectively, stabilized the model. The simulation started on 1 June 2017 and ran for 200 days. Hourly wind and pressure from a 3-km resolution data-assimilating model (HRRR; Benjamin et al. 2016) forced the simulation. Wind stress was computed using wind speed relative to surface currents

$$\tau_s = \rho_a C_D |\mathbf{u}_{10} - \mathbf{u}_{\text{mix}}| (\mathbf{u}_{10} - \mathbf{u}_{\text{mix}}) \quad (17)$$

where $\rho_a = 1.22 \text{ kg m}^{-3}$ is the air density, \mathbf{u}_{10} is the wind velocity 10-m above the surface, and C_D is a drag coefficient computed from Large and Pond (1981).

c. Observations

Water level gauges provide a critical ground truth for dynamical models of SSH. Since at least 1970, hourly water level data have been collected by NOAA at Duluth, Grand Marais, Ontonogan, and Point Iroquois (<https://tidesandcurrents.noaa.gov/>) and by Fisheries and Oceans Canada at Thunder Bay, Rossport, Michipicoten, and Gros Cap (<https://www.waterlevels.gc.ca>). Since Gros Cap and Point Iroquois are only separated by a few kilometers, we only analyze data at Point Iroquois. Hourly data at Marquette are available from NOAA starting in 1980.

In order to examine water level hydrodynamics, it is necessary to remove the (spatial) mean water level, which depends on the hydrological cycle. We define mean water level as the 14-day running mean of the 8-station average. Mean lake level has large inter-annual variability and an annual cycle (Lenters 2001) with 14 cm amplitude (28 cm range) and high water on September 8 (Fig. 2a). After removing mean water level from each station, the remaining data displayed long-term cross-lake tilting due to postglacial rebound (not shown, but see Mainville and Craymer 2005). Linear least-squares regression indicated that Duluth is sinking at 27 cm/century and Michipicoten is rising at 22 cm/century, consistent with prior estimates by Mainville and Craymer

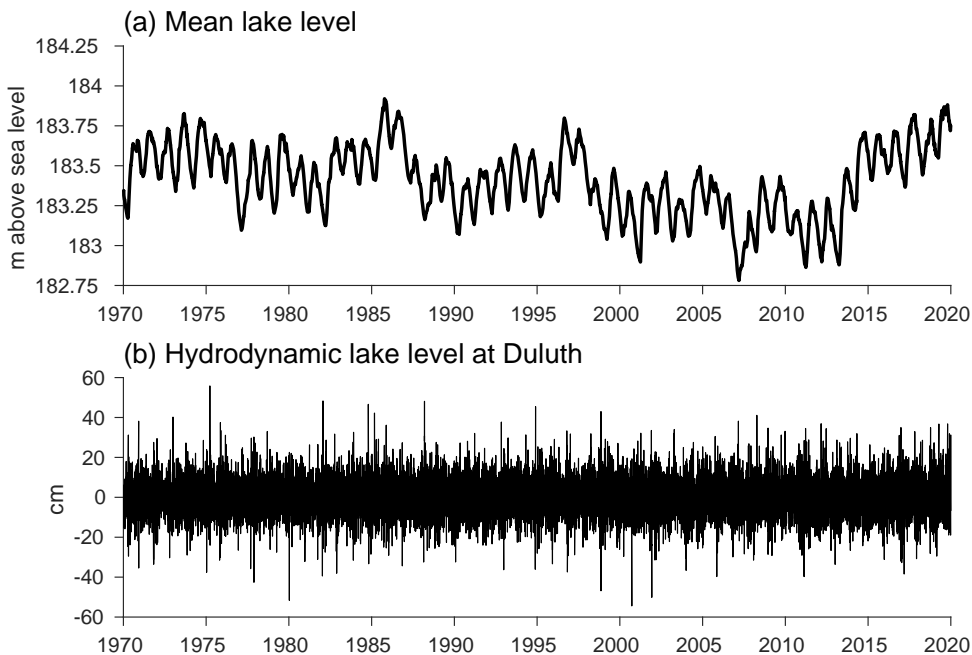


FIG. 2. Mean lake level (a) and hydrodynamical water level at Duluth (b)

(2005). After removing post glacial rebound, the remaining signal is hydrodynamical water level, which we simply call “water level”. Note that water level is not high-pass filtered at each station, however, removing the (low-passed spatial) mean water level and post glacial rebound eliminates most variability at timescales longer than a week.

We briefly examine sub-surface velocity using the Western Mooring (WM) deployment from 14 July - 17 October 2017 at 185 m depth in the western arm of Lake Superior (Austin and Elmer 2022), next to NOAA buoy 45006 (Fig. 1). The mooring had an upward-looking acoustic Doppler current profiler (ADCP) in an inline cage at 78.5 m depth, which recorded horizontal current velocity every 10 minutes in 2 m bins to the surface. We removed near surface data that was contamination by surface reflections. At each time, we projected the vertical structure of velocity onto vertical modes following Thomson and Emery (2014). We then computed power spectra from the vertical mode amplitudes to identify peaks at the natural frequencies of gravity modes. We did not identify any peaks associated with reduced-gravity (baroclinic) basin modes because these modes have periods of a month or longer, and seasonal stratification evolves significantly over this time scale.

3. Modeling Results

a. The MITgcm Simulation

Raw SSH, atmospheric pressure, and windstress from the MITgcm simulation were projected onto the first 10 (super-inertial) gravity modes, which explained 94% of SSH variance. The SSH projection was dominated by the first and second modes, which explained 66% and 11% of the SSH variance each, respectively. Similarly, 96% percent of atmospheric pressure variance was explained by the first 10 modes, with 68% and 13% explained by the first two modes. This result indicates that atmospheric pressure primarily forces gravity modes and not the mean circulation. Conversely, only 72% of wind stress was explained by the first ten modes, with 25% and 16% explained by the first two modes. This result indicates that the wind forces both gravity modes and the mean circulation.

Snapshots of SSH reconstructed from the first 10 gravity modes resemble an east-west seiche (Fig. 3). Removing the gravity modes reveals a residual SSH that looks like a streamfunction (i.e., it has nearly constant values along the coastline). To further isolate the streamfunction, we remove the atmospheric pressure that does not project onto the gravity modes, which is essentially a modified inverted barometer correction.

The gravity modes in the MITgcm simulation evolve as prototypical oscillators with resonant amplitude peaks at the natural frequencies and strong coherence between the forcing (F_n) and response (A_n ; Figs. 4 and 5). As expected, the response transitions from in-phase to out-of phase with the forcing as the frequency passes the natural frequency. A consequence of these dynamics is that low-frequency atmospheric forcing drives a substantial low-frequency SSH response, even though it is well below resonance. That is, atmospheric forcing can slowly tilt the lake or cause it to rapidly seiche.

b. The Harmonic Oscillator Model

We test the harmonic oscillator model by solving for A_n using (15) and comparing it with the fully nonlinear MITgcm. We force the harmonic oscillator using F_n computed from the same wind and pressure that was also used to force the MITgcm, except ignoring the impact of surface currents on wind stress in (17). The damping parameter was tuned during a brief parameter sweep and

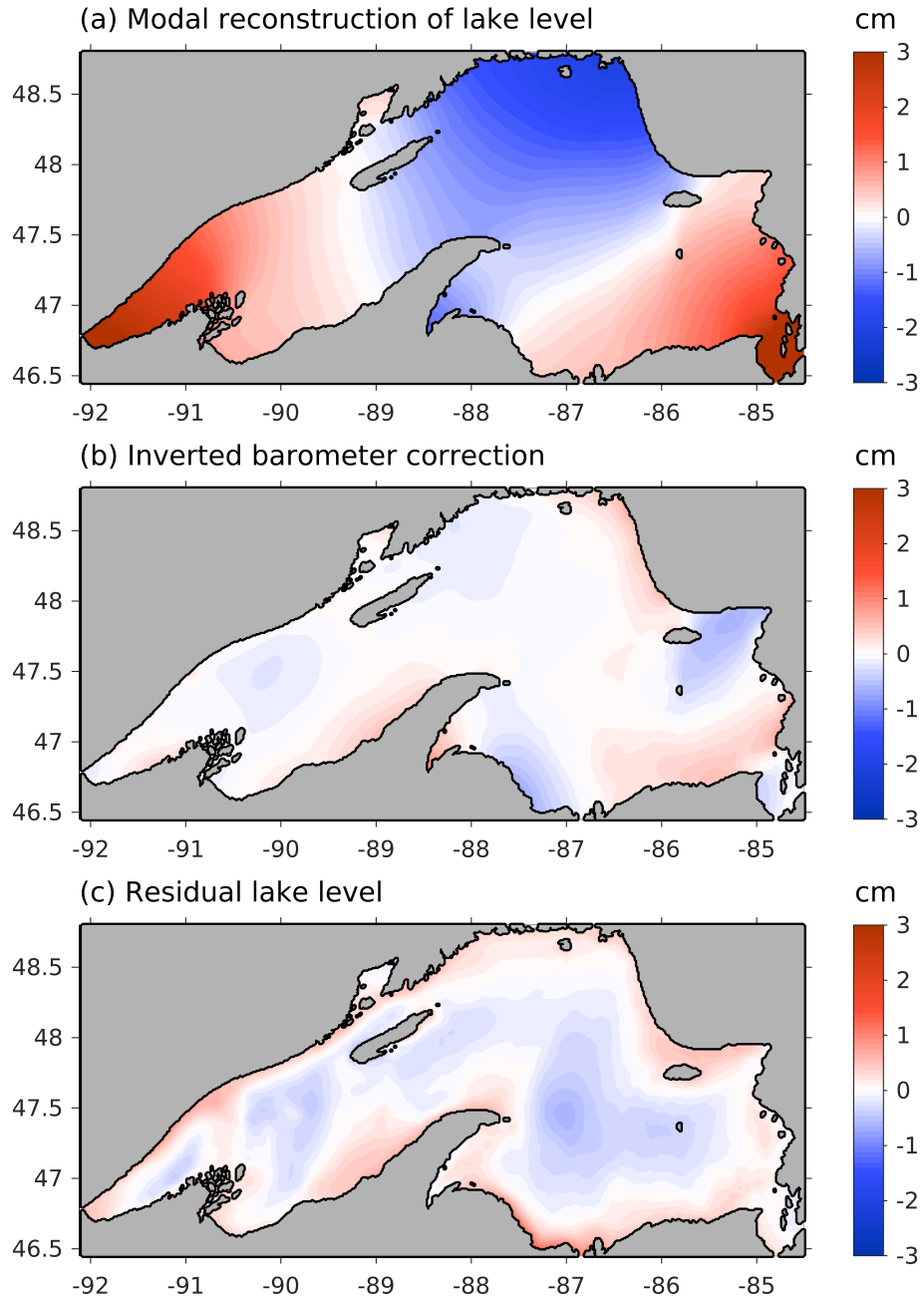


FIG. 3. Simulated snapshots of SSH on 16 July 2017 due to gravity modes (a), the inverted barometer (b), and residual (c). Here, the inverted barometer is just the atmospheric pressure that does not project onto gravity modes. Residual SSH is nearly identical to estimates of geostrophic SSH determined from time-averaging (cf. Fig. 8).

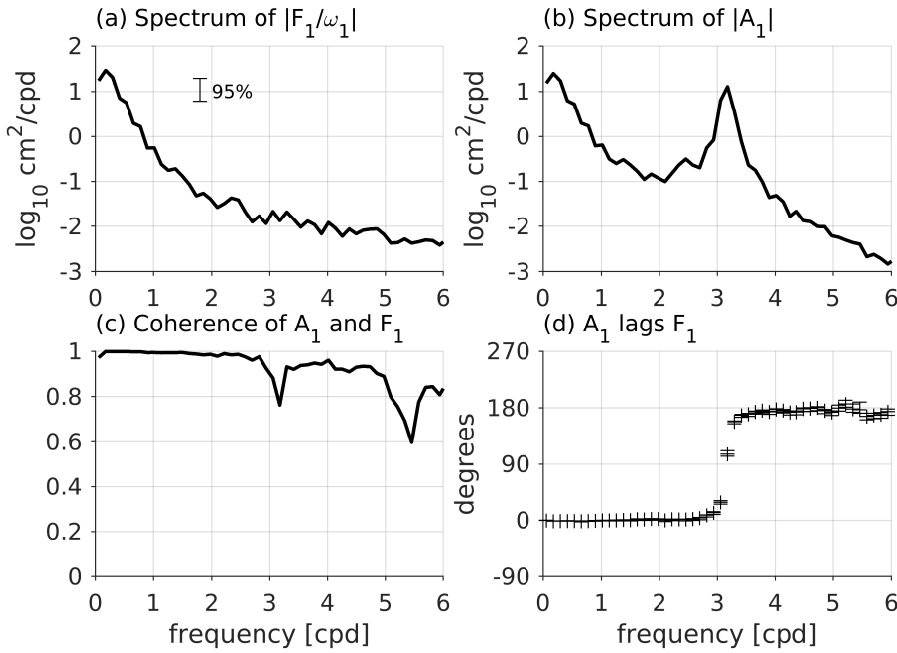


FIG. 4. The power spectral density of mode-1 forcing (a) is red, while that of mode-1 amplitude (b) is peaked at the natural frequency (3 cpd). The forcing and modal amplitude are highly coherent (c) and become out of phase at the natural frequency (d). The 95% confidence interval is shown (Chelton 2015) and all data is band-averaged to produce 48 degrees of freedom (DOF). Forcing is divided by frequency so that it has the same dimensions as modal amplitude.

eventually implemented as $r_n = n^2 / (2.5 \text{ days})$. In general, the exact drag formulation had little impact on results and additional experiments with quadratic drag did not improve the results.

The harmonic oscillator model explains 96% and 87% of variance in the mode-1 and mode-2 amplitudes obtained from the MITgcm. Timeseries of the mode-1 amplitudes from each model are nearly indistinguishable, and the amplitudes are highly coherent with zero phase lag (Fig. 6). The agreement is notable because the MITgcm simulations have substantially more realistic physics than (15). The MITgcm includes (non-linear) advection, quadratic bottom drag, stratification, the β effect, and wind stress computed from relative wind. However, ignoring these dynamics when deriving (15) does not significantly degrade its predictive power.

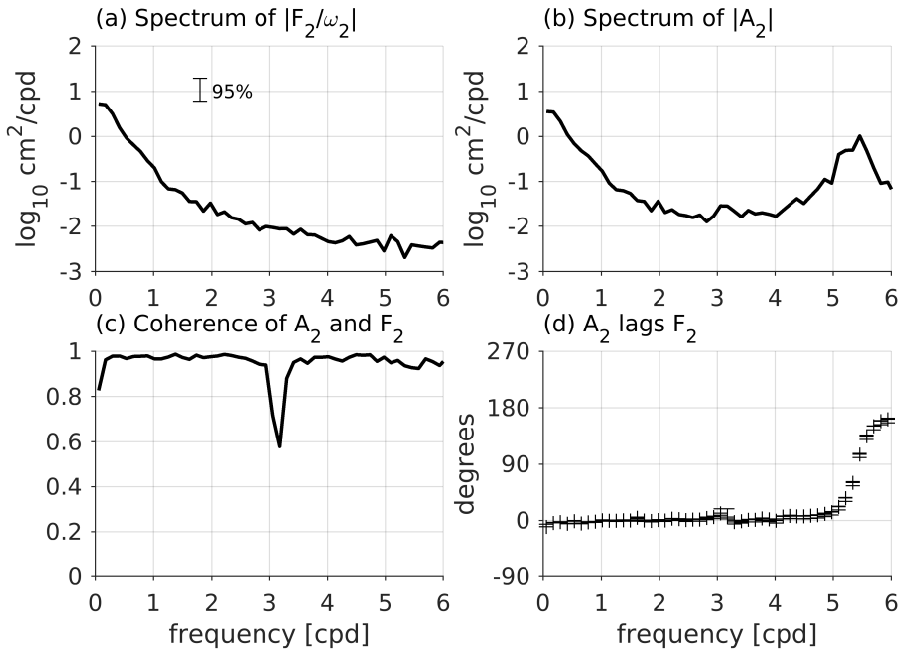


FIG. 5. As in Fig. 4, except for mode 2 (5 cpd).

c. Seiche Energetics

To identify what drives the gravity modes, we quantified the rates of work by atmospheric pressure and wind stress using the oscillator model (Fig. 7). Atmospheric pressure (0.07 mW m^{-2}) is more important than wind stress (0.01 mW m^{-2}), although both rates of work are small compared to, say, near-inertial wind work, which can reach $\mathcal{O}(1 \text{ mW m}^{-2})$ (E. Green, personal communication). Gravity mode energy (1.6 J m^{-2}) is mostly mode-1 because it has the weakest damping. Gravity mode energy is much weaker than near-inertial energy during the stratified season, which is $\mathcal{O}(10^2 \text{ J m}^{-2})$ (Austin 2013). That is, barotropic gravity modes in Lake Superior produce weak currents and do not dissipate sufficient power to mix the lake during the stratified season.

d. Filtering Seiches From Instantaneous SSH

Gravity modes represent noise in satellite estimates of geostrophic SSH. The harmonic oscillator model effectively filters gravity modes from snapshots of SSH, providing a simple alternative to Carrere and Lyard (2003) for large lakes and enclosed seas. In Lake Superior, subtracting just the first two modes gravity modes from instantaneous SSH, removes 89% of the gravity-mode variance in instantaneous SSH and produces SSH fields that closely resemble time-averaged, geostrophic

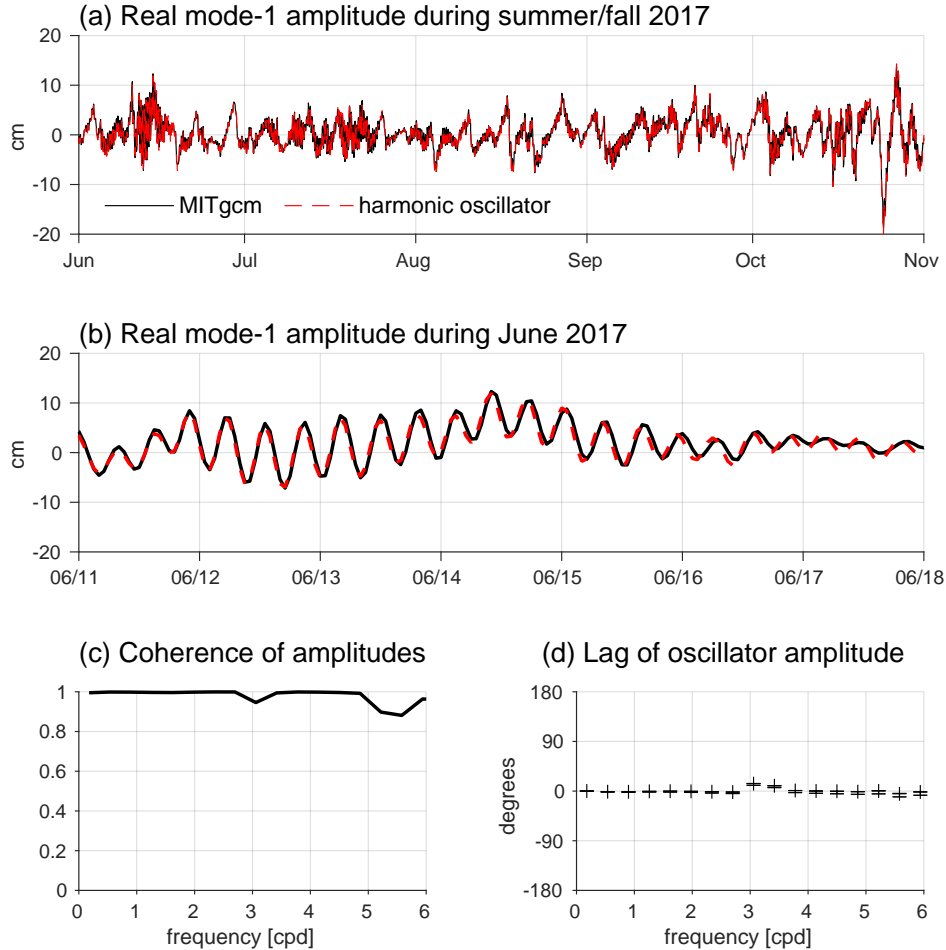


FIG. 6. The mode-1 amplitude from the MITgcm and harmonic oscillator are nearly identical over a 5 month period (a) and over an individual week (b). The amplitudes are highly coherent (c) with a phase lag of zero (d). Note that the amplitude is complex (representing an amplitude and phase), but only the real part, which is equivalent to a time series at Duluth, is shown in (a) and (b).

SSH (Fig. 8). The impact of this correction can be seen on 16 July 2017, where the east-west SSH gradient in the gravity mode at 89° W would falsely imply a southward geostrophic jet, were it not removed.

4. Observational Results

The preceding section establishes that gravity modes in an MITgcm simulation are highly predictable from the harmonic oscillator model (15). Here we examine in situ observations of gravity

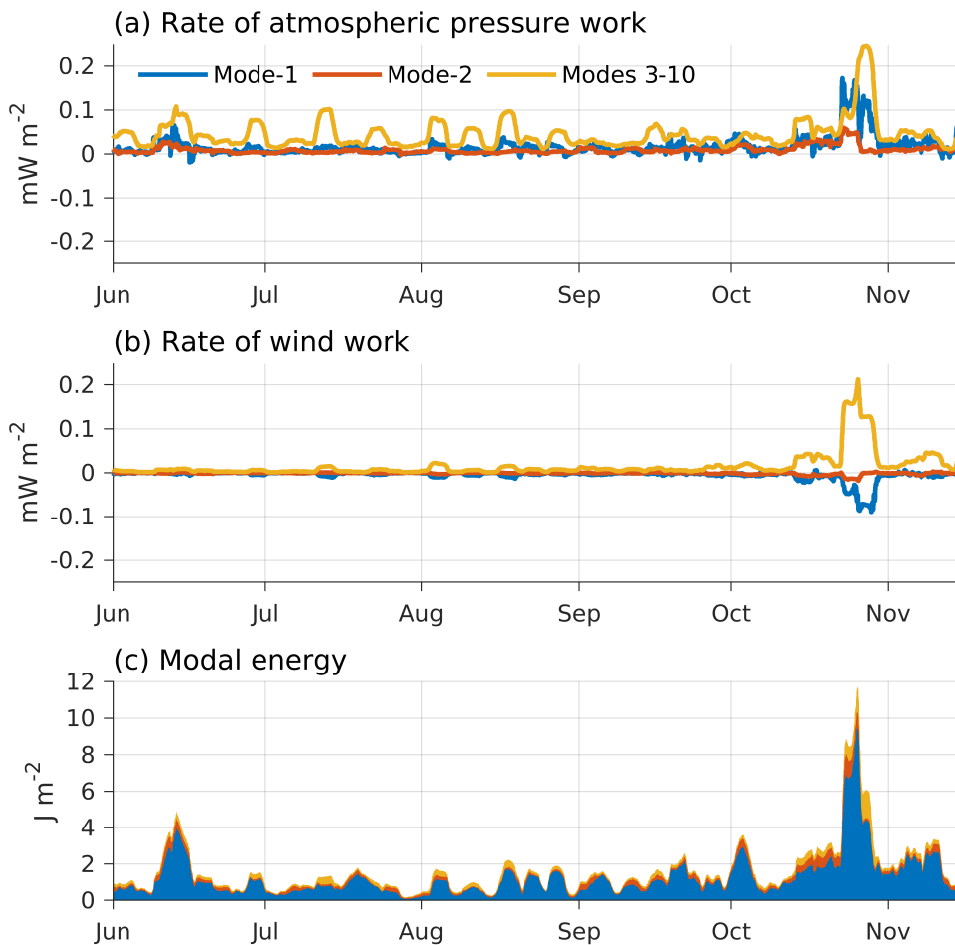


FIG. 7. The rate of work by atmospheric pressure (a) and wind stress (b) is temporally intermittent and spread across several modes, but energy (c) is dominated by mode 1.

modes in Lake Superior to determine if they are also consistent with the the harmonic oscillator model.

a. SSH spectra

Water level at Duluth has an amplitude of about 10 cm, with occasional spikes of 50 cm (Fig. 2b). SSH frequency spectra are red with narrow peaks at 1 and 2 cpd due to astronomical tides and broad peaks at 3 and 5 cpd due to basin modes (Fig. 9). Duluth is located at an anti-node for the first basin mode (Fig. 1b), explaining the prominent peak at 3 cpd. In contrast, Rossport is located near a node, and has a much smaller peak at 3 cpd. Both Duluth and Rossport are located

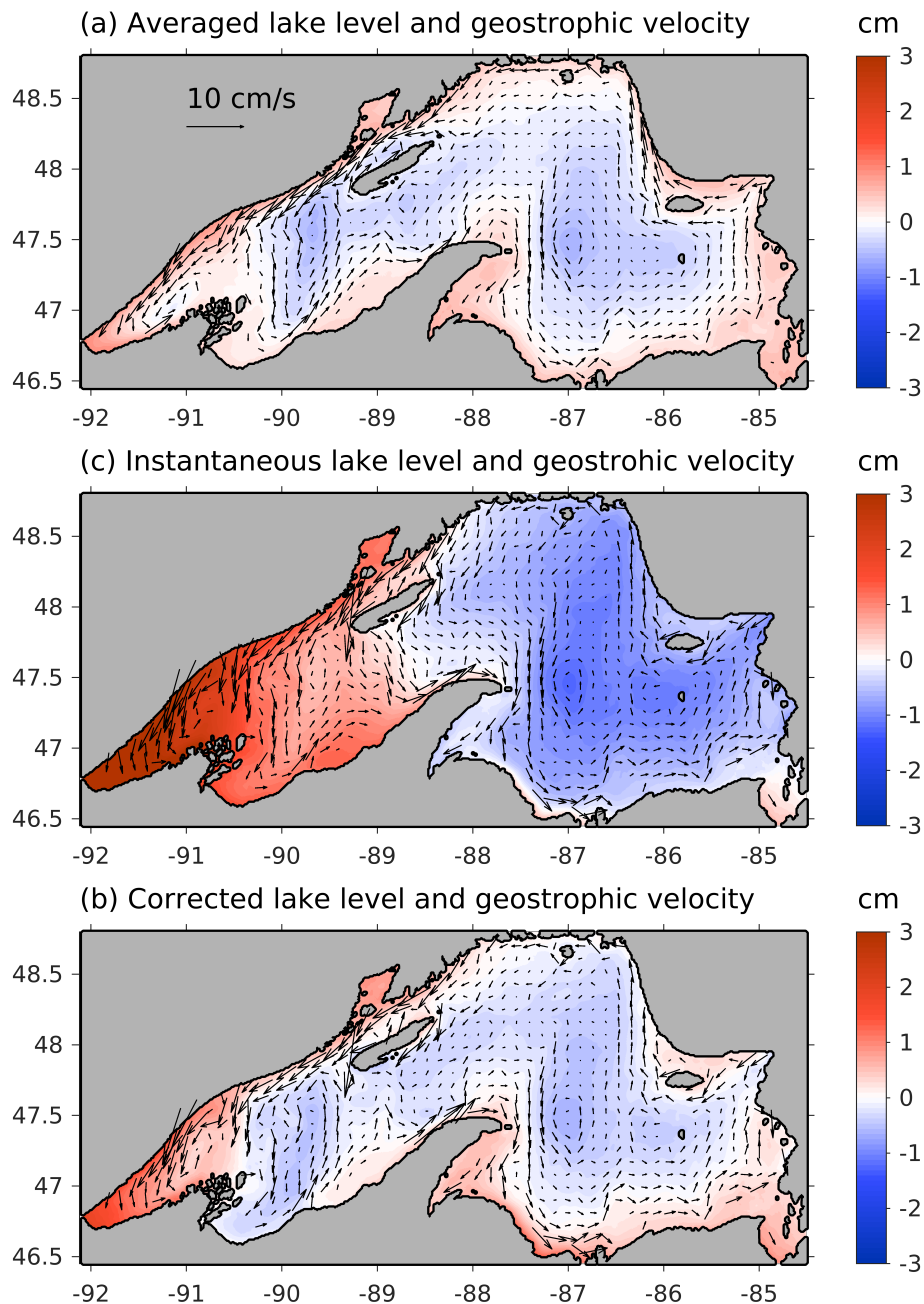


FIG. 8. SSH and surface currents averaged over 160 h (a) differ from instantaneous fields (b) on 16 July 2017.

A “corrected” SSH (c) that resembles averaged SSH is obtained by removing the first two gravity modes predicted by the harmonic oscillator model. Atmospheric pressure is removed from all SSH maps. Surface currents are computed from each SSH field assuming the geostrophic balance. This is a poor assumption for instantaneous SSH (b) because it contains gravity modes.

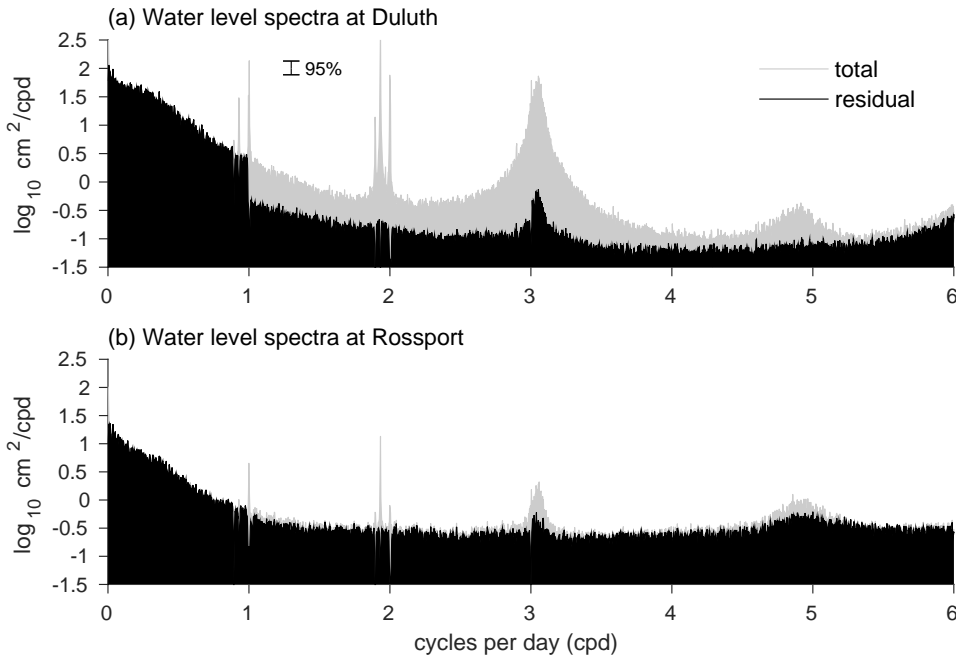


FIG. 9. Water level spectra at Duluth (a) and Rossport (b). Removing tides and the first two CEOFs (above 1 cpd) from the water level produces a residual water level that is 1-2 orders of magnitude smaller than the total. The 95% confidence interval is shown (100 DOF)

near anti-nodes in the second mode (Fig. 1c), which has a frequency of 4.9 cpd (Rao and Schwab 1976).

b. Vertical structure

Frequency power spectra of velocity from WM during summer 2017 are dominated by baroclinic (vertical mode 1) near-inertial oscillations at 1.5 cpd that rotate clockwise (Fig. 10). Austin (2013) described baroclinic near-inertial motions in Lake Superior, showing that the summer stratification is approximately two-layered and flow speeds in the upper layer routinely exceed 10 cm s^{-1} . Austin (2013) attributed the velocity peak at 3 cpd as the first gravity mode (seiche). We suggest this peak is a harmonic of the inertial peak because (i) the peak is baroclinic (vertical mode 1), while gravity modes are barotropic (vertical mode 0), and (ii) the peak is highly polarized (like an inertial oscillation), while gravity modes are weakly polarized. Instead, we attribute the much smaller vertical mode-0 peak at 3 cpd as the first gravity mode because it is barotropic and rotates equally clockwise and counter clockwise. Thus, seiche kinetic energy is three orders of magnitude smaller

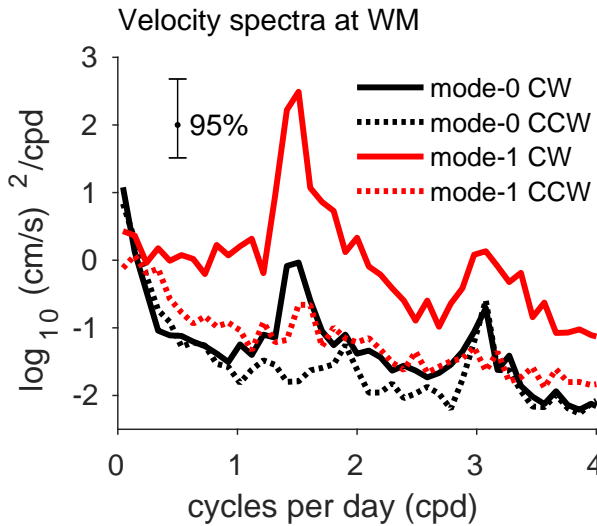


FIG. 10. Rotary spectra from summer 2017 of the vertical mode-0 (barotropic; black) and vertical mode-1 (baroclinic; red) velocity amplitudes at WM, which was located next to NOAA buoy 45006. The 95% confidence interval is shown (18 DOF).

than near-inertial kinetic energy and one order of magnitude smaller than the first harmonic of near-inertial kinetic energy.

c. Tides

Lake Superior has small but easily quantifiable tides (Fig. 9), which were analyzed in detail by Mortimer and Fee (1976) and Sanchez et al. (1985). They are predictable from (12) because the tidal potential is well known and straightforward to project onto modes. This was the procedure of Platzman (1984a) in the world oceans and Sanchez et al. (1985) in Lake Superior. Sanchez et al. (1985) found that the first basin mode alone explained 95% of the variance in the M₂ (12.4 h) tide. Since we are focused on variability due to atmospheric forcing, we simply removed the tides by fitting harmonic constants over 120 day increments and linearly interpolating the constants to each observational time. This procedure ensures that most non-stationary tides are removed (Kelly et al. 2015), regardless of whether they arise from physical processes or slight movements of the gauges. Tidal variances ranged from 4.6 cm² at Duluth to 0.4 cm² at Marquette (Table 1).

Station	total	tide	seiche	mode-1	mode-2	residual
Duluth	36.8	4.6	6.8	6.1	0.7	0.6
Grand Marais	11.8	1.4	3.7	2.7	0.2	0.9
Thunder Bay	11.2	0.9	1.5	0.7	0.0	0.8
Rosport	9.3	1.1	1.7	0.1	0.3	1.3
Michipicoten	20.7	2.0	3.4	1.5	0.0	1.6
Pt. Iroquois	40.8	2.7	7.8	4.4	2.6	0.2
Marquette	11.0	0.4	2.0	0.7	0.1	1.3
Ontonagan	9.5	1.2	2.4	1.1	0.2	1.1

TABLE 1. Summary of water level variances in cm^2 at eight stations (see Fig. 1). Tidal variance is estimated from 120 day harmonic fits. The “seiche” is de-tided variability between 1-6 cpd. The mode 1 and 2 signals are the 1-6 cpd data projected onto the first and second CEOF, respectively. The residual is the 1-6 cpd signal after removing tides, mode 1, and mode 2. Averaged across all stations, modes 1 and 2 describe 73% of seiche variance (i.e., 2.7 of 3.7 cm^2).

d. Observed vs. simulated SSH

Observed water level at Duluth agrees with the MITgcm simulation over multi-day timescales, but not shorter timescales (Fig. 11). For example, below 1 cpd the simulation is 80% coherent with the observations, but this drops to 50% and 20% at the natural frequencies of the first (3 cpd) and second (5 cpd) modes, respectively (Fig. 11c). Despite losing coherence, the two time series remain largely in phase (Fig. 11d), suggesting the model forcing (i.e., the HRRR reanalysis) is statistically noisy at higher frequencies. NOAA buoys provide more accurate forcing at a few points, but do not resolve the spatial structure needed to determine F_n from (13). In summary, gravity modes are predictable from atmospheric reanalysis at low frequencies (< 1 cpd), but not higher frequencies.

e. Observed Modal Amplitudes

To observe the amplitudes of the gravity modes at higher frequencies, we must fit the modes to the observations at the 8 gauges (Fig. 1). This is challenging because the modes are orthogonal with respect to a basin-wide integral (9) that is difficult to approximate with just 8 points. One possibility is to fit modes 1 and 2 to the 8 stations at each hourly interval using least-squares regression. This method risks over-fitting because there are only 4 degrees of freedom (8 stations minus two amplitudes and phases). Instead, we incorporate frequency information into the fit

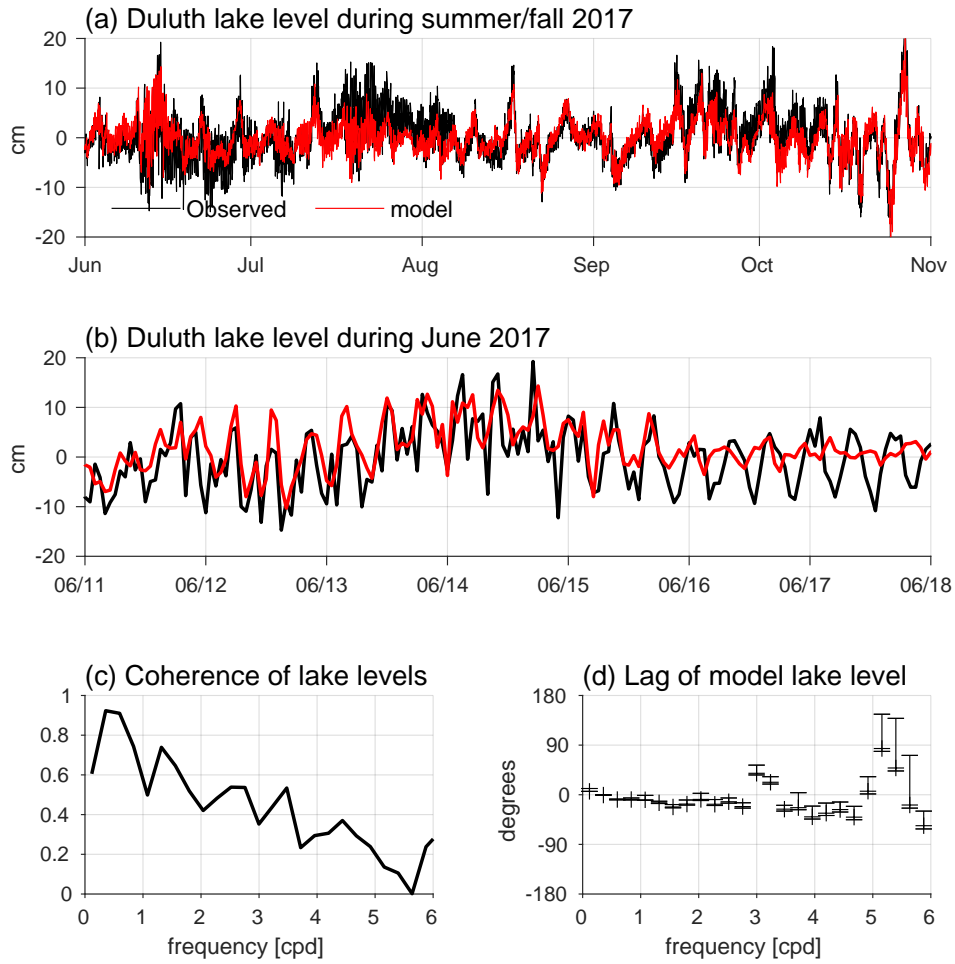


FIG. 11. Observed and MITgcm lake level display similar weekly trends (a), but often disagree on daily timescales (b). The coherence between the observed and modeled lake levels decreases at higher frequencies(c), although the time series remain in phase (d).

by bandpassing the data around the mode-1 and mode-2 natural frequencies (2.95-3.15 cpd and 4.80-5.00 cpd) and then computing the complex empirical orthogonal functions (CEOFs; Barnett 1983). We chose CEOFs instead of traditional EOFs so that we could identify the amplitude and phase of propagating signals (numerous “flavors” of EOFs are discussed in Thomson and Emery 2014). The CEOF calculation is essentially a systematic refinement of Mortimer and Fee (1976)’s method of determining optimal station phases “by inspection, giving greater weight to station pairs showing high interstation coherence”. The resulting CEOF shapes are nearly identical to the basin modes, explaining 94% and 78% of the spatial variance in the first two modes across the

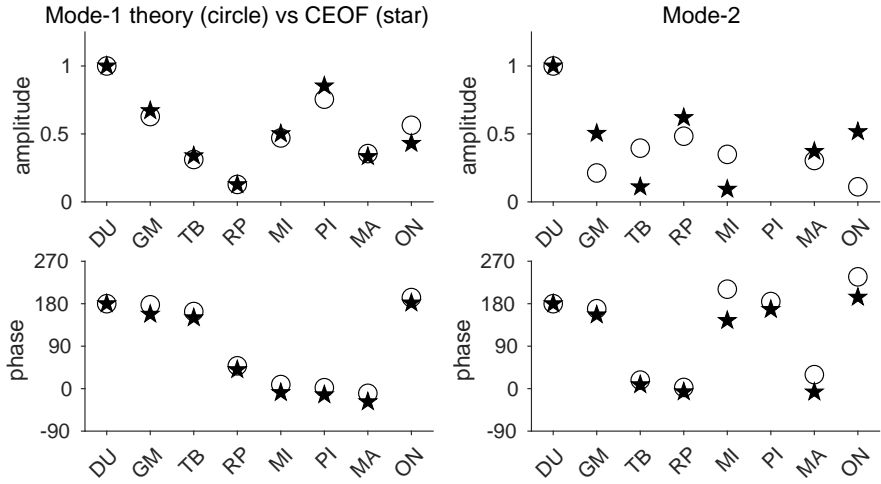


FIG. 12. First (left) and second (right) observed (CEOF) and theoretical basin modes amplitude (top) and phase (bottom). The CEOF explains 94% and 78% of variance in the first and second modes, respectively.

8 observed locations (Fig. 12). The first CEOF is also consistent with previous observations of seiche amplitude and phase (Mortimer and Fee 1976).

CEOFs are orthogonal (by definition) across the 8 observational stations at any given instant, so we project the full time series onto them at each instant to obtain the mode-1 and 2 CEOF amplitudes. Because the CEOF and gravity mode shapes are functionally identical at the 8 lake-level gauges (Fig. 12), we simply refer to the CEOF amplitudes as the “modal amplitudes”. Low frequency (< 1 cpd) modal amplitudes are predictable from HRRR reanalysis, so we only analyze the observed amplitudes at 1-6 cpd. As expected, the mode 1 and 2 amplitudes explain the spectral peaks at 3 and 5 cpd, respectively (Fig. 9). They also explain about 74% of lake level variance in the seiche frequency band (1-6 cpd; Table 1). For example, variance in the seiche-band is about 6.8 cm² at Duluth, and all but 0.6 cm² is explained by the first two gravity modes. Time series of the seiche-band lake level and the mode 1+2 reconstruction at Duluth are nearly identical (Fig. 13).

f. Observed modal dynamics

Observed A_1 and A_2 are hypothesized to evolve as damped, forced harmonic oscillators. If the wind spectrum is reasonably flat near the resonant frequency, the harmonic oscillator model

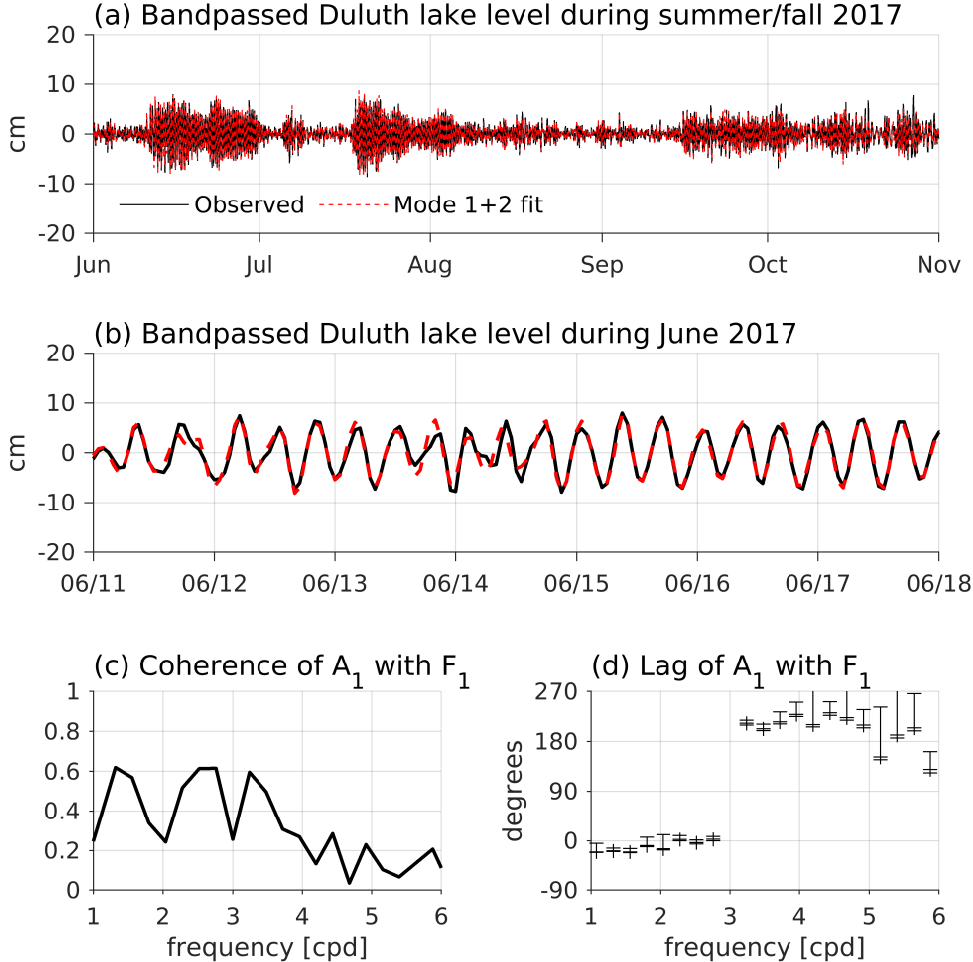


FIG. 13. Total and mode 1+2 lake level (bandpassed at 1–6 cpd) are difficult to distinguish on monthly (a) and daily timescales (b). The mode-1 amplitude is only 20–60% coherent with HRRR reanalysis forcing (F_1), although the phase relation is consistent with a harmonic oscillator (d; cf. Fig. 4d).

predicts an amplitude spectrum of the form

$$\frac{C}{1 + (\omega_n - \omega)^2 / r_n^2} \quad (18)$$

where C is an amplitude constant (e.g., Morse 1948). The power spectra of A_1 and A_2 , computed from 50 years of data, closely resemble this shape, confirming the harmonic oscillator interpretation (Fig. 14). Fits to the spectral model (see e.g., Colosi and Munk 2006) using nonlinear least squares

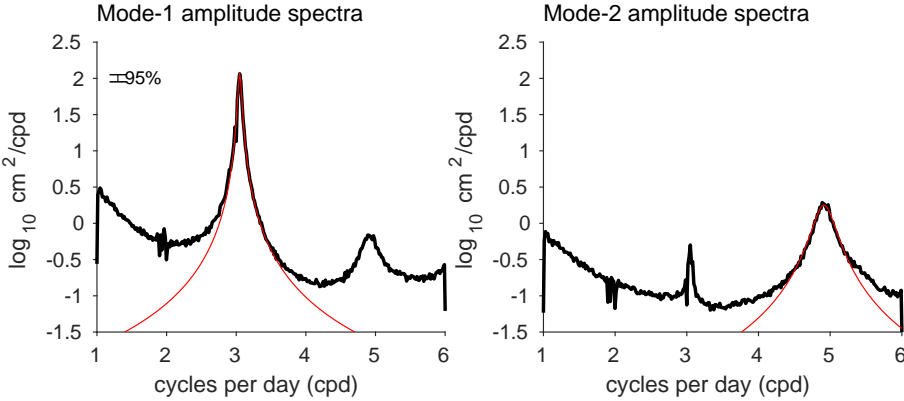


FIG. 14. Power spectra of the mode-1 (a) and mode-2 (b) amplitudes (A_1 and A_2). The mode has been re-scaled so that amplitude indicates displacement at Duluth. The red curve is a best-fit Lorentzian curve (18). The 95% confidence interval is shown (600 DOF).

(Matlab's `lsqcurvefit.m` function) indicate $\omega_1 = 3.05$ cpd, $\omega_2 = 4.91$ cpd, $r_1^{-1} = 5.9$ days, and $r_2^{-1} = 1.0$ days.

Observed modal amplitudes exhibit spectral shapes consistent with harmonic oscillators, suggesting they should be predictable given accurate atmospheric forcing. Unfortunately, A_1 is only 20-60% coherent with F_1 (computed from HRRR reanalysis), even though their phasing is consistent with a driven harmonic oscillator (cf. Figs. 4d and 13d). These results reiterate that the HRRR reanalysis is too noisy above 1 cpd to consistently predict the amplitude and phase of the seiche. Although, the HRRR reanalysis does generate the right amount of seiche energy in the general circulation model and has even successfully replicated meteotsunamis produced by specific storms (Anderson and Mann 2021).

Observed lake-wide energy in the mode-1 and 2 seiche is 2.2 J m^{-2} and 0.4 J m^{-2} (lake-wide integrals are 184 GJ and 34 GJ), similar to the model (Section 3c). Assuming a steady state balance in (16), the rate of work/dissipation is 0.01 mW m^{-2} (1 MW total) for both mode 1 and 2, slightly less than modeled (Section 3c). Dissipation is the same for both modes because the decrease in energy from mode 1 to mode 2 is compensated by the increase in the drag coefficient from mode 1 to mode 2.

The gravity modes are driven by atmospheric forcing and should therefore vary in time due to intermittent storms and seasonal climatology. Cumulative probability distributions reveal $|A_1| < 5$

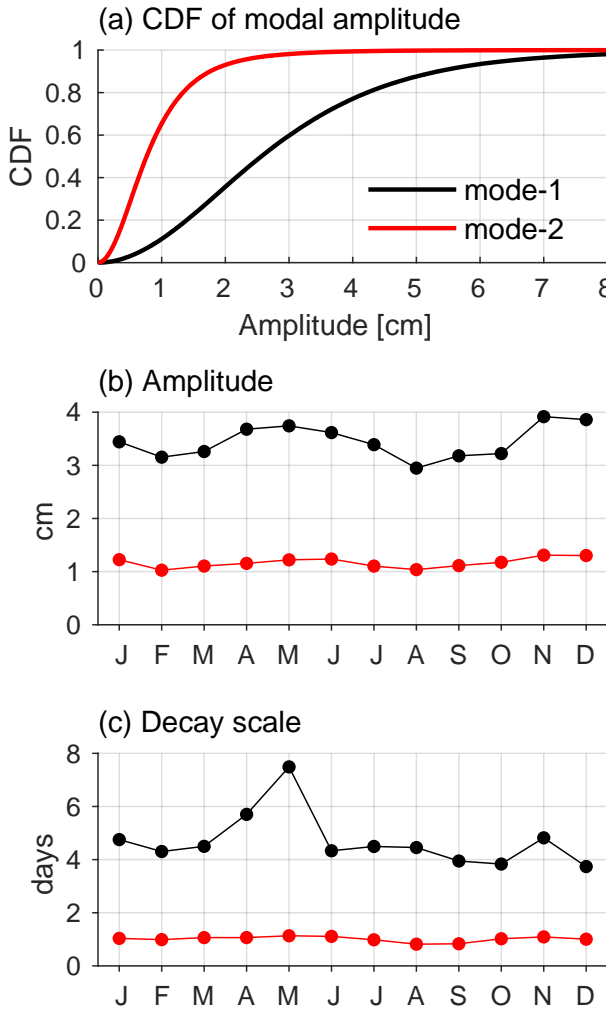


FIG. 15. Cumulative distribution function (CDF) of observed modal amplitudes between 1-6 cpd (a). Average monthly mode-1 amplitudes, $|A_n|$ (b), and decay timescales, r_n^{-1} (c). Amplitudes are re-scaled to indicate displacement at Duluth.

cm and $|A_2| < 2$ cm about 90% of the time in the seiche band (1-6 cpd; Fig. 15a). Amplitudes are nearly constant throughout the year, with monthly averages of A_1 only increasing by about 0.5 cm during the stormier spring and fall months. The decay scale is also constant throughout the year ($r_1^{-1} \approx 4.5$ days and $r_2^{-1} \approx 1.0$ days), except for an anomalous increase in r_1^{-1} to 7.5 days during May that defies explanation. Additional analyses (not shown) failed to identify any other seasonal trends, for example, ω_1 does not increase with mean lake level following Merian's formula and r_1 does not increase with seiche amplitude due to non-linear (quadratic) bottom drag.

5. Conclusions

Most SSH variability (94%) in a simulation of Lake Superior is associated with the first 10 basin-wide gravity modes. These modes describe both low-frequency tilting (the inverted barometer) and high-frequency oscillations (seiching). CEOF analysis of 8 lake-level gauges identifies patterns consistent with the first and second gravity modes (Fig. 12). The two observed modes explain 73% of observed SSH variance between 1-6 cpd. Observations of higher-mode structures are limited by the spatial resolution of the gauge network and presence of high-frequency (> 6 cpd) local harbor modes. Gravity modes produce substantial SSH signals but contain and dissipate very little kinetic energy (about 2.6 J m^{-2} and 0.02 mW m^{-2} , respectively), so they have little impact on currents or mixing.

Gravity modes theoretically evolve as forced damped oscillators. This theory explained 96% and 87% the variance of modes 1 and 2 in a realistic general circulation model of Lake Superior (Fig. 6). Specifically, the inclusion of nonlinear advection, stratification, quadratic bottom drag, relative wind stress, and latitudinal variability in the inertial frequency do not greatly alter the evolution of the first two gravity modes. Observed mode 1 and 2 amplitudes also have frequency spectra consistent with harmonic oscillators. They display characteristic peaks at the natural frequencies (3.05 cpd and 4.91 cpd; Fig. 14) and an abrupt change in phase with the atmospheric forcing above the natural frequency (cf. Figs. 4d and 13d). The observed spectra also imply drag coefficients of approximately $r_1^{-1} \approx 4.5$ days and $r_2^{-1} \approx 1.0$ days. For reference, these drag coefficients indicate quality factors of $Q_1 = 43$ and $Q_2 = 16$. the latter is similar to the global surface tide (Carwright and Ray 1991).

Gravity modes are driven by atmospheric pressure gradients and, to a lesser extent, wind (Fig. 7). The net forcing, F_n , is governed by how well pressure and wind patterns project on to each mode [i.e., the integral in (13)]. Like any harmonic oscillator, impulsive forcing (due to a sudden storm) can excite a broad-band response, while periodic forcing (due an oscillating wind-stress or traveling storm) can produce a narrow-band response. Analogously, a pendulum can excited by striking it abruptly, slowly pushing it up and down, or periodically bumping it.

The coherence of observed mode-1 amplitude, A_1 , with with the HRRR reanalysis, F_1 , is high (80%) at low frequencies (< 1 cpd), indicating that the reanalysis product can accurately predict basin-wide tilting due to gravity modes. Unfortunately, A_1 and F_1 are only 50% coherent at the

natural frequency of the first mode (3.05 cpd; Fig. 13c), so large near-resonant motions are poorly predicted by the HRRR reanalysis. This failure is simply due to the requirement of high spatial accuracy at high frequencies. Even the coherence of A_1 with buoy observations is low (50%, not shown) at 3 cpd, because most atmospheric variability at this frequency does not match the shape of the first gravity mode (furthermore, the buoy network is too sparse to observe the spatial pattern). A mismatch between the spatial patterns of atmospheric forcing and gravity modes is even more common in large basins, likely explaining why resonant modes are not observed in the global ocean (Luther 1983; Platzman 1984b).

This study provides guidance for creating a dynamic atmosphere correction for SWOT observations of Lake Superior. At low frequencies (< 1 cpd), the HRRR-reanalysis can be used to either force a general circulation model or the harmonic oscillator model. If a general circulation model is used, the simulated SSH can be projected onto gravity modes. At higher frequencies (1-6 cpd), uncertainties in the wind forcing require that the mode-1 and mode-2 amplitudes be determined from lake-level gauges. Fitting the lake-level gauges to gravity modes using CEOFs is simply a way of extrapolating the gauge measurements to the entire lake. This reconstruction is optimal in a least-squares sense because it prioritizes the orthogonal modes with the largest amplitudes (e.g., Wunsch 2006). After combining the high- and low-frequency gravity modes, the dynamic atmosphere correction should be modified to include the inverted barometer response due to the time-averaged atmospheric pressure that does not project onto gravity modes, as this pressure is not accounted for by the gravity-mode model. Our proposed dynamic atmosphere correction (applied to a simulation in Fig. 8) hinges on the agreement between instantaneous SWOT data and lake-level gauges, which we will evaluate in the future.

Appendix

Equation (9) contrasts the simpler orthogonality conditions for modes in non-rotating ($f = 0$) basins:

$$\frac{1}{A} \int \eta_m \eta_n dA = \delta_{mn} \quad \text{and} \quad \frac{1}{A} \int \mathbf{U}_m \cdot \mathbf{U}_n dA = \delta_{mn}. \quad (19)$$

The non-rotating case is simpler because η_n doubles as a scalar potential for the transport, allowing the problem to be rewritten as a single equation in η_n with the no-flow boundary condition expressed

$\hat{\mathbf{n}} \cdot \nabla \eta_n = 0$ (the problem can also be re-written as a single equation in \mathbf{U}_n). The accompanying proof of orthogonality is straightforward following the steps in Section 2. Conversely, re-writing the rotating ($f \neq 0$) system as a single equation in η_n results in a boundary condition that contains the eigenvalue: $\hat{\mathbf{n}} \cdot \nabla \eta_n + if/\omega_n \hat{\mathbf{t}} \cdot \nabla \eta_n = 0$ where $\hat{\mathbf{t}}$ is the unit vector tangent to the boundary. In essence, rotation allows a cross-shore surface slope to the extent that it is compensated by an along-shore geostrophic current. The presence of ω_n in the boundary condition makes the eigenvalue problem “irregular” (Rao and Schwab 1976), a term that foreshadows difficulty ahead.

It is standard to analyze modes in a flat bottom cylinder from a single equation involving η (Lamb 1945; Wunsch 2015). The solutions are

$$\eta_{ln} = J_l(k_n r) e^{il\phi} \quad (20a)$$

$$U_{ln} = \frac{igH}{\omega_n^2 - f^2} \left(fl \frac{\eta_{ln}}{r} - \omega_n \partial_r \eta_{ln} \right) \quad (20b)$$

$$V_{ln} = \frac{gH}{\omega_n^2 - f^2} \left(\omega l \frac{\eta_{ln}}{r} - f \partial_r \eta_{ln} \right) \quad (20c)$$

where r and ϕ are the radial and azimuthal coordinates, $\mathbf{U}_{ln} = (U_{ln} \hat{\mathbf{r}}, V_{ln} \hat{\phi})$, l is the azimuthal mode number, J_l is the l^{th} order Bessel function of the first kind, and k_n is the wavenumber, which is related to frequency through the dispersion relation $\omega_n^2 = k_n^2 g H + f^2$. The eigenfrequencies are determined by numerically solving for k_n using the boundary condition at $r = r_0$,

$$k_n r_0 J'_l(k_n r_0) - \frac{lf}{\sqrt{k_n^2 g H + f^2}} J_l(k_n r_0) = 0 \quad (21)$$

where $J'_l = \partial_z J_l(z)$. Attempting to leverage a well-known orthogonality property of Bessel functions, Wunsch (2015) incorrectly states that η_n are orthogonal via

$$\int_0^{r_0} J_l(k_m r) J_l(k_n r) r dr = \delta_{mn}. \quad (22)$$

Unfortunately, the above equation is only satisfied when $J'_l(k_n r_0) = 0$ or $J_l(k_n r_0) = 0$, a condition that is only true if $f = 0$ or $\omega_n = 0$ in (21). The correct orthogonality condition is (9), which can be verified by substituting (20) and integrating numerically. We also attempted to verify the orthogonality condition (9) analytically by substituting (20) and exploiting the many known

properties of Bessel functions, but such a proof eluded us. Despite the confusion, (22) is a good approximation of (9) for parameters relevant to Lake Superior, yielding terms that are $\mathcal{O}(10^{-2})$ when $m \neq n$.

Acknowledgments. Kelly was supported by NASA grant 80NSSC20K1331 and National Science Foundation grant OCE-1635560. Green was also supported by National Science Foundation grant OCE-1635560. Mansur was supported by the University of Minnesota Duluth Physics & Astronomy Department and Water Resources Sciences program. C. Wunsch provided insightful comments on an earlier draft. Three anonymous reviewers improved the paper with insightful comments.

Data availability statement. The code for solving the eigenvalue problem, the MITgcm setup files, post-processing scripts, and plotting scripts are available at the Data Repository of University of Minnesota (DRUM; doi: TBD).

References

- Ahmed, S., C. D. Troy, and N. Hawley, 2014: Spatial structure of internal Poincaré waves in Lake Michigan. *Environ. Fluid Mech.*, **14**, 1229–1249.
- Anderson, E. J., A. J. Bechle, C. H. Wu, D. S. Schwab, G. E. Mann, and K. A. Lombardy, 2015: Reconstruction of a meteotsunami in Lake Erie on 27 May 2012: Roles of atmospheric conditions on hydrodynamic response in enclosed basins. *J. Geophys. Res.*, **120**, 8020–8038.
- Anderson, E. J., and G. E. Mann, 2021: A high-amplitude atmospheric inertia–gravity wave-induced meteotsunami in Lake Michigan. *Natural Hazards*, **106**, 1489–1501.
- Anderson, E. J., and D. S. Schwab, 2013: Predicting the oscillating bi-directional exchange flow in the Straits of Mackinac. *J. Great Lakes Res.*, **39**, 663–671.
- Anderson, E. J., and D. S. Schwab, 2017: Meteorological influence on summertime baroclinic exchange in the Straits of Mackinac. *J. Geophys. Res.*, **122**, 2171–2182.
- Angove, M., and Coauthors, 2021: Addressing the meteotsunami risk in the United States. *Natural Hazards*, **106**, 1467–1487.

- Antenucci, J. P., and J. Imberger, 2001: Energetics of long internal gravity waves in large lakes. *Limnol. Oceanogr.*, **46**, 1760–1773.
- As-Salek, J. A., and D. J. Schwab, 2004: High-frequency water level fluctuations in Lake Michigan. *J. Waterway, Port, Coastal, Ocean Eng.*, **130**, 45–53.
- Austin, J. A., 2013: Observations of near-inertial energy in Lake Superior. *Limnol. Oceanogr.*, **58**, 715–728.
- Austin, J. A., and J. Allen, 2011: Sensitivity of summer Lake Superior thermal structure to meteorological forcing. *Limnol. Oceanogr.*, **56**, 1141–1154.
- Austin, J. A., and C. Elmer, 2022: An archive of lake superior temperature and current measurements, 2005–2020. *Limnol. Oceanogr. Lett.*
- Barnett, T. P., 1983: Interaction of the monsoon and Pacific trade wind system at interannual time scales. Part I: the equatorial zone. *Mon. Weather Rev.*, **111**, 756–773.
- Bechle, A. J., C. H. Wu, D. A. R. Kristovich, E. J. Anderson, D. J. Schwab, and A. B. Rabinovich, 2016: Meteotsunamis in the Laurentian Great Lakes. *Scientific Reports*, **6**, 37 832.
- Beletsky, D., N. Hawley, and Y. Rao, 2013: Modeling summer circulation and thermal structure of Lake Erie. *J. Geophys. Res.*, **118**, 6238–6252.
- Beletsky, D., J. H. Saylor, and D. Schwab, 1999: Mean circulation of the Great Lakes. *J. Great Lakes Res.*, **25**, 78–93.
- Benjamin, S. G., and Coauthors, 2016: A north american hourly assimilation and model forecast cycle: The rapid refresh. *Mon. Weather Rev.*, **144**, 1669–1694.
- Bennington, V., G. A. McKinley, N. Kimura, and C. H. Wu, 2010: General circulation of Lake Superior: Mean, variability, and trends from 1979 to 2006. *J. Geophys. Res.*, **115**, C12 015.
- Boyce, F. M., M. Donelan, P. Hamblin, C. Murthy, and T. Simons, 1989: Thermal structure and circulation in the Great Lakes. *Atmosphere-Ocean*, **27**, 607–642.
- Boyd, J. P., 2001: *Chebyshev and Fourier Spectral Methods*. 2nd ed., Dover Publications, 668 pp.

- Carrere, L., and F. Lyard, 2003: Modeling the barotropic response of the global ocean to atmospheric wind and pressure forcing - comparisons with observations. *Geophys. Res. Lett.*, **30**, 1275.
- Carwright, D. E., and R. D. Ray, 1991: Energetics of global ocean tides from geosat altimetry. *J. Geophys. Res.*, **96**, C01 059.
- Chelton, D., 2015: Lecture notes: A short course on time series analysis. IMEDEA (CSIC-UIB), Mallorca, Spain.
- Colosi, J. A., and W. Munk, 2006: Tales of the venerable Honolulu tide gauge. *J. Phys. Oceanogr.*, **36**, 967–996.
- Cox, K., E. Brocious, S. C. Courtenay, M. R. Vinson, and S. A. Mason, 2021: Distribution, abundance and spatial variability of microplastic pollution on the surface of Lake Superior. *J. Great Lakes Res.*, **47**, 1358–1364.
- Csanady, G. T., 1982: *Circulation in the coastal ocean*. Springer, 279 pp.
- Cushman-Roisin, B., and J.-M. Beckers, 2011: *Introduction to Geophysical Fluid Dynamics*. 2nd ed., Academic Press, 875 pp.
- Duhaut, T. H. A., and D. N. Straub, 2006: Wind stress dependence on ocean surface velocity: Implications for mechanical energy input to ocean circulation. *J. Phys. Oceanogr.*, **36**, 202–211.
- Egbert, G. D., 1997: Tidal data inversion: Interpolation and inference. *Prog. in Oceanogr.*, **40**, 81–108.
- Egbert, G. D., A. F. Bennett, and M. G. G. Foreman, 1994: TOPEX/POSEIDON tides estimated using a global inverse model. *J. Geophys. Res.*, **99**, C12 24,821–24,852.
- Ewing, M., F. Press, and W. L. Donn, 1954: An explanation of the Lake Michigan wave of 26 june 1954. *Science*, **120**, 684–686.
- Hamblin, P. F., and E. Hollan, 1978: On the gravitational seiches of Lake Constance and their generation. *Schweiz. Z. Hydrol.*, **40**, 119–154.
- Hutter, K., Y. Wang, and I. P. Chubarenko, 2011: *Physics of Lakes Volume 2: Lakes as Oscillators*. Springer, 646 pp.

- Jordan, T. F., K. R. Stortz, and M. Sydor, 1981: Resonant oscillations in Duluth-Superior Harbor. *Limnol. Oceanogr.*, **26**, 186–190.
- Kelly, S. M., N. L. Jones, G. I. Ivey, and R. N. Lowe, 2015: Internal tide spectroscopy and prediction in the Timor Sea. *J. Phys. Oceanogr.*, **45**, 64–83.
- Kumambala, P. G., and A. Ervine, 2010: Water balance model of Lake Malawi and its sensitivity to climate change. *Open Hydrology J.*, **4**, 152–162.
- Lamb, H., 1945: *Hydrodynamics*. 6th ed., Dover, 768 pp.
- Large, W. G., and S. Pond, 1981: Open ocean momentum flux measurements in moderate to strong winds. *J. Phys. Oceanogr.*, **11**, 324–336.
- Le Traon, P.-Y., and R. Morrow, 2001: Ocean currents and eddies. *Satellite Altimetry and Earth Sciences: A Handbook for techniques and Applications*, L.-L. Fu, and A. Cazenave, Eds., Academic Press, San Diego, 171–210.
- Lebedev, S., 2018: Climatic variability of water circulation in the Caspian Sea based on satellite altimetry data. *Inter. J. Remote Sensing*, **39**, 4343–4359.
- Lenters, J. D., 2001: Long-term trends in the seasonal cycle of great lakes water levels. *J. Great Lakes Res.*, **27**, 342–353.
- Luther, D., 1983: Why haven't you seen an ocean mode lately? *Ocean Modelling*, **50**, 1–6.
- MacKinnon, J. A., and K. B. Winters, 2005: Subtropical catastrophe: Significant loss of low-mode tidal energy at 28.9° . *Geophys. Res. Lett.*, **32**, L15 605.
- Mainville, A., and M. R. Craymer, 2005: Present-day tilting of the Great Lakes region based on water level gauges. *Geological Society of America Bulletin*, **117**, 1070–1080.
- Marshall, J., A. Adcroft, C. Hill, L. Perelman, and C. Heisey, 1997: A finite-volume, incompressible Navier-Stokes model for studies of the ocean on parallel computers. *J. Geophys. Res.*, **102**, 5753–5766.
- Meadows, G. A., L. A. Meadows, W. L. Wood, J. M. Hubertz, and M. Perlin, 1997: The relationship between Great Lakes water levels, wave energies, and shoreline damage. *Bulletin of the American Meteorological Society*, **78**, 675–683.

- Miles, J. W., 1974: Harbor seiching. *Annual Rev. Fluid Mech.*, **6**, 17–33.
- Monserrat, S., I. Vilivic, and A. B. Rabinovich, 2006: Meteotsunamis: atmospherically induced destructive ocean waves in the tsunami frequency band. *Nat. Hazards Earth Syst. Sci.*, **6**, 1035–1051.
- Morris, C. S., and S. K. Gill, 1994: Evaluation of the TOPEX/POSEIDON altimeter system over the Great Lakes. *J. Geophys. Res.*, **99**, 24 527–24 539.
- Morrow, R., and Coauthors, 2019: Global observations of fine-scale ocean surface topography with the Surface Water and Ocean Topography (SWOT) mission. *Frontiers Mar. Sci.*, **6**, Article 232.
- Morse, P. M., 1948: *Vibration and sound*. Acoustical Society of America.
- Mortimer, C. H., 2006: Inertial oscillations and related internal beat pulsations and surges in Lakes Michigan and Ontario. *Limnol. Oceanogr.*, **51**, 1941–1955.
- Mortimer, C. H., and E. J. Fee, 1976: Free surface oscillations and tides of Lakes Michigan and Superior. *Phil. Trans. Roy. Soc. London A*, **281**, 1–61.
- Nevers, M. B., M. N. Byappanahalli, T. A. Edge, and R. K. Whitman, 2014: Beach science in the Great Lakes. *J. Great Lakes Res.*, **40**, 1–14.
- Nicholls, R. J., and A. Cazenave, 2010: Sea-level rise and its impact on coastal zones. *Science*, **328**, 1517–1520.
- Platzman, G. W., 1972: Two dimensional free oscillations in natural basins. *J. Phys. Oceanogr.*, **2**, 117–132.
- Platzman, G. W., 1984a: Normal modes of the world ocean. Part III: A procedure for tidal synthesis. *J. Phys. Oceanogr.*, **14**, 1521–1531.
- Platzman, G. W., 1984b: Normal modes of the world ocean. Part IV: Synthesis of diurnal and semidiurnal tides. *J. Phys. Oceanogr.*, **14**, 1532–1550.
- Pollard, R. T., and R. C. Millard, 1970: Comparison between observed and simulated wind-generated inertial oscillations. *Deep-Sea Res.*, **17**, 813–821.

- Prange, M., T. Wilke, and F. P. Wesselingh, 2020: The other side of sea level change. *Communications Earth & Environment*, **1**, 1–4.
- Rao, D. B., 1966: Free gravitational oscillations in rotating rectangular basins. *J. Fluid Mech.*, **23**, 523–555.
- Rao, D. B., and D. J. Schwab, 1976: Two dimensional normal modes in arbitrary enclosed basins on a rotating Earth: Application to Lakes Ontario and Superior. *Phil. Trans. R. Soc. Lond. A*, **281**, 63–96.
- Rao, D. B., and D. J. Schwab, 1981: A method of objective analysis for currents in a lake with application to Lake Ontario. *J. Phys. Oceanogr.*, **11**, 739–750.
- Rao, D. B., S. D. Steenrod, and B. V. Sanchez, 1987: A method of calculating the total flow from a given sea surface topography. *NASA Tech. Memorandum*, 87799.
- Remucal, C. K., 2002: Spatial and temporal variability of perfluoroalkyl substances in the Laurentian Great Lakes. *Environ. Sci.: Processes Impacts*, **21**, 1816–1834.
- Rueda, F. J., and S. G. Schladow, 2002: Surface seiches in lakes of complex geometry. *Limn. Oceanogr.*, **47**, 906–910.
- Sanchez, B. V., D. B. Rao, and P. G. Wolfson, 1985: Objective analysis for tides in a closed basin. *Marine Geodesy*, **9**, 71–91.
- Sayers, M. J., A. G. Grimm, R. A. Shuchman, K. R. Bosse, G. K. Fahnenstiel, S. A. Rudberg, and G. A. Leshkevich, 2019: Satellite monitoring of harmful algal blooms in the Western Basin of Lake Erie: A 20-year time-series. *J. Great Lakes Res.*, **13**, 508–521.
- Saylor, J. H., and G. S. Miller, 1987: Studies of large-scale currents in Lake Erie, 1979-80. *J. Great Lakes Res.*, **13**, 487–514.
- Schwab, D. J., 1977: Internal free oscillations in Lake Ontario. *Limn. Oceanogr.*, **22**, 700–708.
- Schwab, D. J., 1980: The free oscillations of lake st. clair: An application of Lanczos procedure. *National Oceanic and Atmospheric Administration Technical Memo*, No. ERL–GLERL–32.
- Schwab, D. J., 1982: An inverse method for determining wind stress from water-level fluctuations. *Dyn. Atmos. Oceans*, **6**, 251–278.

- Shimizu, K., and J. Imberger, 2008: Energetics and damping of basin-scale internal waves in a strongly stratified lake. *Limnol. Oceanogr.*, **53**, 1574–1588.
- Shimizu, K., J. Imberger, and M. Kumagai, 2007: Horizontal structure and excitation of primary motions in a strongly stratified lake. *Limnol. Oceanogr.*, **52**, 2641–2655.
- Simons, T. J., and W. M. Schertzer, 1989: Modeling wind-induced water setup in Lake St. Clair. *J. Great Lakes Res.*, **15**, 452–464.
- Smith, W. H. F., and D. T. Sandwell, 1997: Global sea floor topography from satellite altimetry and ship depth soundings. *Science*, **277**, 1956–1962.
- Steinmoeller, D. T., M. Stastna, and K. G. Lamb, 2019: Calculating basin-scale free oscillations in lakes on a rotating Earth. *Ocean Modelling*, **139**, 101 403.
- Taqi, A. M., A. M. Al-subhi, M. A. Alsaafani, and C. P. Abdulla, 2019: Estimation of geostrophic current in the Red Sea based on sea level anomalies derived from extended satellite altimetry data. *Ocean Sci.*, **15**, 017 508, doi:10.1063/1.3273 054.
- Thomson, R. E., and W. J. Emery, 2014: *Data Analysis Methods in Physical Oceanography*. 3rd ed., Elsevier, 716 pp. pp.
- Trebitz, A. S., 2006: Characterizing seiche and tide-driven daily water level fluctuations affecting coastal ecosystems of the great lakes. *J. Great Lakes Res.*, **32**, 102–116.
- Valiour, R., D. Bouffard, L. Boegmann, and Y. R. Rao, 2015: Near-inertial waves in Lake Erie. *Limnol. Oceanogr.*, **60**, 1522–1535.
- Woodworth, P. L., and Coauthors, 2019: Forcing factors affecting sea level changes at the coast. *Surveys in Geophysics*, **40**, 1351–1397.
- Wunsch, C., 2006: *Discrete inverse and state estimation problems: with geophysical fluid applications*. 384 pp.
- Wunsch, C., 2015: *Modern observational physical oceanography: understanding the global ocean*. Princeton University Press.
- Wunsch, C., and D. Stammer, 1997: Atmospheric loading and the oceanic “inverted barometer” effect. *Reviews of Geophysics*, **35**, 79–107.